Impact of irradiation conditions on the magnetic field sensitivity of spin defects in hBN nano flakes

Saksham Mahajan,¹ Ravi Kumar,² Aferdita Xhameni,¹ Gautham Venu,¹ Basanta Mistri,^{3, a)} Felix Donaldson,² T. Taniguchi,⁴ K. Watanabe,⁵ Siddharth Dhomkar,^{2,3,a)} Antonio Lombardo,^{1,2} and John J.L. Morton^{1,2}

(*Electronic mail: saksham.mahajan@ucl.ac.uk)

(Dated: 17 October 2025)

We study V_B^- centres generated by helium focused ion beam (FIB) irradiation in thin (\sim 70 nm) hBN nanoflakes, in order to investigate the effect of implantation conditions on the key parameters that influence the magnetic field sensitivity of V_B^- quantum sensors. Using a combination of photoluminescence, optically detected magnetic resonance, and Raman spectroscopy we examine the competing factors of maximising signal intensity through larger V_B^- concentration against the degradation in spin coherence and lattice quality observed at high ion fluences. Our results indicate that both the V_B^- spin properties and hBN lattice parameters are largely preserved up to an ion fluence of 10^{14} ions/cm², and beyond this significant degradation occurs in both. At the optimal implantation dose, an AC magnetic sensitivity of $\sim 1 \mu T/\sqrt{Hz}$ is achieved. Using the patterned implantation enabled by the FIB we find that V_B^- centres and the associated lattice damage are well localized to the implanted regions. This work demonstrates how careful selection of fabrication parameters can be used to optimise the properties of V_B^- centres in hBN, supporting their application as quantum sensors based in 2D materials.

I. INTRODUCTION

Optically active point defects in solid-state materials have long attracted interest for the development of quantum technologies¹⁻⁷ due to their long quantum coherence times, simple measurement protocols and scalability. For instance, point defects in three-dimensional materials, such as color centres in diamond⁸, have been widely explored for nanoscale quantum sensing with applications ranging from probing current distributions in materials such as graphene⁹ to in-situ studies of biological systems, including single proteins¹⁰ and living cells¹¹. Although such point defects offer lower absolute magnetic field sensitivity than state of the art sensors like SQUIDs $(\eta_{mag} \sim 1 \text{ fT/}\sqrt{Hz})^{12}$, their atomistic nature and presence within wide band gap materials enables higher spatial resolution, and robust operation across a broad temperature range. To take advantage of such enhanced spatial resolution, these defects must be positioned close to the surface, where interactions with surface-related noise sources degrade quantum coherence and ultimately limit sensitivity.

As a potential solution to the limitations of surface noise on the performance of quantum sensors in three-dimensional materials like diamond, wide bandgap van der Waals (2D) materials have been explored as hosts for addressable quantum systems. Among these, the negatively charged boron vacancy (V_B^-) centre in hexagonal boron nitride (hBN) has been identified as an optically addressable spin^{6,13} with the ability to

sense various external physical stimuli such as electric and magnetic fields, temperature and pressure¹⁴. Despite their short coherence time (Hahn echo $T_2 < 100 \text{ ns}$)^{15,16} arising from the hBN nuclear spin bath, and their low quantum efficiency ($\sim 0.03\%$)¹⁷, the prospect of being able to position optically addressable spins in 2D materials with sub-nanometer proximity to the target sample offers potential advantages for sensing applications.

Boron-vacancy centres can be created using ion implantation, which offers advantages such as spatial localization through use of a focused ion beam (FIB) and improved repeatability compared to alternative methods ¹⁸. Prior studies have successfully demonstrated the creation of $V_{\rm B}^-$ centres using a variety of ions (H, He, Ga, N)^{19–21} under different implantation conditions. These implantation parameters must be carefully optimized to achieve a high concentration of $V_{\rm B}^-$ centres while maintaining the hBN crystallinity. Although a higher concentration of $V_{\rm B}^-$ centres enhances signal intensity which, in principle, improves magnetic field sensitivity, increasing the implantation fluence can affect spin coherence time and introduce lattice damage, which hinders the fabrication of hBN based heterostructures.

In this study, we employ helium FIB at various doses to form $V_{\rm B}^-$ centres in hBN and then study their spin and optical properties. We evaluate how varying ion fluence alters factors such as count rate, coherence, optical contrast, and the extent of lattice damage, which ultimately contribute to the $V_{\rm B}^-$ magnetic field sensitivity. FIB implantation was performed using low energy He⁺ ions (25 keV) across a range of ion fluences (10¹² to 10¹⁵ ions/cm²) in hBN nanoflakes with thickness \sim 70 nm. Helium ions were preferred due to their low atomic

¹⁾Department of Electrical and Electronic Engineering, UCL, London WC1E 7JE, UK.

²⁾London Centre for Nanotechnology, UCL, 17-19 Gordon St, London WC1H 0AH, UK.

³⁾Department of Physics, Indian Institute of Technology Madras, Chennai 600036, India

⁴⁾Research Center for Materials Nanoarchitectonics, National Institute for Materials Science, 1-1 Namiki, Tsukuba 305-0044, Japan

⁵⁾Research Center for Electronic and Optical Materials, National Institute for Materials Science, 1-1 Namiki, Tsukuba 305-0044, Japan

a) Also at Center for Quantum Information, Communication and Computing, Indian Institute of Technology Madras, Chennai 600036, India

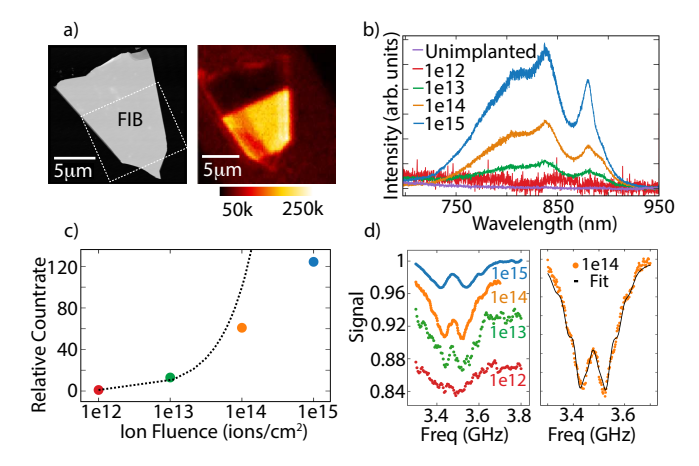


FIG. 1. Fabrication and optical characterization of $V_{\rm B}^-$ centres in hBN nanoflakes. a) AFM (left) and fluorescence confocal image (right) of a sample irradiated with an ion fluence of $10^{14}~{\rm cm}^{-2}$. The interfaces between implanted and unimplanted regions are visible in the confocal image. b) PL spectra of unimplanted and implanted samples, with the latter showing characteristic $V_{\rm B}^-$ emissions centered around $\sim 820~{\rm nm}$. To aid comparison of spectral features, the PL spectra of samples 1e12 and 1e13 have been scaled in amplitude by a factor of 10 and 2, respectively. c) Relative fluorescence intensity (calculated from PL spectra) of different samples with dotted line representing linear increase in counts with ion fluence. d) Pulsed ODMR spectra (left) along with fitted data for sample 1e14 (right) using the theoretical model (for details, see SI).

mass, which minimizes lattice damage²² and their ability to introduce a high density of point defects²². Photoluminescence (PL), spin resonance, and Raman spectroscopy reveal a correlation between reduced coherence times and increased lattice disorder. The optimum AC magnetic field sensitivity (approximately 1 $\mu T/\sqrt{Hz}$) was achieved at an ion fluence of 10^{14} ions/cm², where hBN crystallinity is preserved. Finally, we analyze the spatial distribution of defects around the patterned implantation interface using PL and Raman spectroscopy.

II. EXPERIMENTAL DETAILS

A. Sample fabrication

The hBN samples were prepared by mechanical exfoliation of bulk crystals which were grown under high pressure and temperature 23 . Subsequently, four hBN nanoflakes with similar thicknesses (~ 70 nm) were identified through atomic force microscopy (Bruker Dimension Icon with ScanAsyst) and an example image is shown in Fig. 1(a). The selected hBN nanoflakes were transferred onto a gold microstrip (thickness 200 nm, width 20 μ m and length 3.5 mm, fabricated on a silicon substrate) for plasmonic enhancement of $V_{\rm B}^-$ related emission 24 as well as efficient microwave delivery. After the flake transfer, $V_{\rm B}^-$ centres were created using FIB (ZEISS ORION NanoFab) implantation of He $^+$ ions (25 keV) with fluences ranging between 10^{12} and 10^{15} ions/cm 2 . Defect dis-

tributions were estimated using Stopping and Range of Ions in Matter (SRIM) calculations (Fig. SI2) with SRIM 2008 software, indicating nearly uniform $V_{\rm B}$ defect concentration along the flake thickness. To enable characterization of the defect distribution around the implantation interface, a portion of the nanoflake was left unimplanted, as illustrated in the confocal image of Fig. 1(a). Below, we refer to the four different samples by the ion fluence used, in ions/cm².

B. Methods

Photoluminescence and optically detected spin measurements were performed using a home-built confocal microscopy setup (NA = 0.65) equipped with a Montana Instruments s100 cryostation and a 522 nm continuous-wave laser (LBX-522: Oxxius). The excitation laser power on different samples varied between 4 and 6 mW. The PL signal was filtered using either a 550 nm or 750 nm long-pass filter (LPF), depending on the experimental requirement, and guided toward either the single-photon counting module (Excelitas Technologies) or the PL spectrometer (SpectraPro HRS500, Princeton Instruments). To investigate the spin properties of the $V_{\rm B}^-$ centres, pulsed optically detected magnetic resonance (PODMR) spectroscopy was performed under zero applied magnetic field. For microwave excitation, a Rohde & Schwarz SGS100A source was modulated through a Swabian Pulse Streamer 8/2. The microwave signal was amplified using a Mini-Circuits amplifier (ZVE-3W-83 +) and delivered to the sample via a gold microstrip wire-bonded to a co-planar waveguide (see Fig. SI3). PODMR spectra were digitally filtered using 35 MHz moving average and fitted using a spin Hamiltonian model (implemented using QuTiP) which incorporates a single boron vacancy coupled to the three first-shell nitrogen atoms^{25,26}. For PODMR fitting, the transition probabilities for all possible spin transitions were calculated using Fermi's Golden Rule. Additional details about the theoretical model are provided in the SI.

Spin-lattice relaxation times (T_1) of V_B^- spins were measured by varying the delay between initialization and readout laser pulses, and spin coherence times (T_2) using a Hahn echo sequence, with phase cycling of the initial pulse to suppress free induction decay (FID) signals superimposed on the decay²⁷. Raman spectra were obtained using a Bruker Senterra II Raman spectrometer system and recorded between $1000-2000~\mathrm{cm^{-1}}$ using 532 nm laser excitation (\sim 2.5 mW of laser power focused through a 0.6 NA objective, resulting in a spot size $< 1 \mu m$). Additionally, to study the point defect-related features (\sim 1290 cm⁻¹) in sample 1e15, multi-wavelength Raman spectroscopy was performed between laser wavelengths of 457-785 nm. For spectral measurements at 457 nm and 514 nm, a separate spectrometer system (Renishaw in Via Raman Microscope, N.A. 0.75, laser power ~ 2 mW) was used.

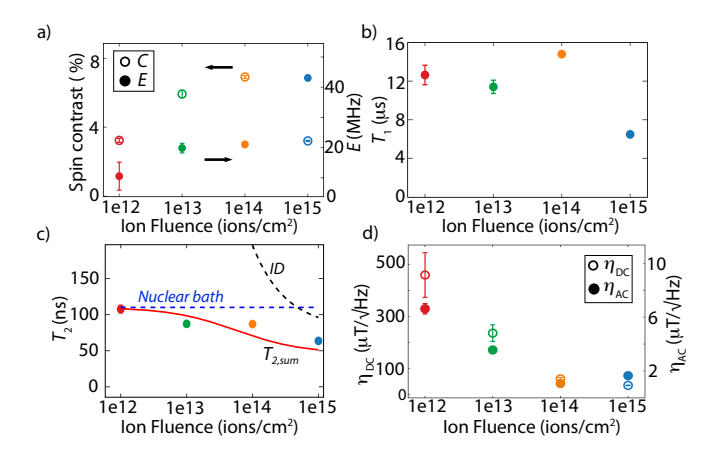


FIG. 2. Spin properties of $V_{\rm B}^-$ centres as a function of ion fluence. a) PODMR contrast (solid circles) and transverse strain splitting parameter (E, open circles). b) Spin-lattice relaxation time, T_1 . (c) The decoherence time T_2 measured by Hahn echo, including various limiting factors: a decoherence rate from the nuclear spin bath (independent of ion fluence), and contributions from instantaneous diffusion (ID) calculated using the model described in the text. d) Estimated AC and DC magnetic sensitivity for the different samples.

III. RESULTS AND DISCUSSION

Photoluminescence spectroscopy (PL) of the FIB implanted flakes (see Fig. 1(b)) reveal the characteristic $V_{\rm B}^-$ related sideband emission with a peak intensity at around 820 nm $^{[13]}$. To investigate dependence of PL signal intensity on ion fluence, each spectrum was integrated over the wavelength range 750–950 nm, and the integrals were normalized to that of the 1e12 sample. The results, shown in Fig. 1 (c), show a sublinear increase in $V_{\rm B}^-$ related PL emission with increasing ion fluence 16 , indicating a reduced conversion efficiency of ions to $V_{\rm B}^-$ centres at fluences above 10^{13} ions/cm 2 .

Pulsed ODMR measurements on each sample exhibit the characteristic resonance of $V_{\rm B}^-$ centres (around 3.5 GHz), as shown in Fig. 1(d)). Fits to the PODMR spectra were used to extract spin Hamiltonian parameters D and E, corresponding to the zero field splitting and strain splitting respectively. While the extracted D was found to be largely independent of ion fluence (see Fig. SI4), the strain splitting E increases monotonically with increasing ion fluence (see Fig. 2(a)). In particular, a significant increase in strain was observed for a fluence of 10¹⁵ ions/cm², indicating a threshold for the formation of extended defects. These extended defects introduced substantial lattice distortion, as confirmed by Raman spectroscopy (discussed further below in Fig. 3. The observed variation in E is consistent with previous reports in which different ion implantation parameters were compared in terms of their effects on spin properties of the $V_{\rm B}^-$ centres^{16,18,28,29}. A further impact of the lattice damage caused at higher ion fluences is seen in the PODMR signal contrast (also shown in (see Fig. 2(a)). The signal contrast initially increases with increasing ion fluence (up to 10^{14} ions/cm²) as the $V_{\rm B}^-$ emission becomes more prominent over the background. However, at the highest fluence of 10^{15} ions/cm², the increased lattice distortion mixes the spin states and reduces the ODMR contrast³⁰. We investigated the spin-lattice relaxation times (T_1) of the different samples (see Fig. 2(b)) and found no significant variation in T_1 up to a fluence of 10^{14} ions/cm². However, T_1 was significantly reduced (halving to $\sim 6~\mu s$) in sample 1e15. This behavior may also be attributed to increased lattice disorder, in this case whereby a resulting anharmonicity in the local phonon density of states enhances phonon-mediated relaxation processes 16,31 .

The performance of $V_{\rm B}^-$ based quantum sensors depends more critically on the spin coherence time, T_2 as these are significantly shorter than T_1 . We measured T_2 using a Hahn echo sequence, which decouples the $V_{\rm B}^-$ centres from the static components of the Ising interaction with surrounding nuclear spins. The resulting decays were well fit by a single exponential decay and the measured T_2 was found to gently decrease with increasing ion fluence across the range of samples studied (see Fig. 2(c)). T_2 in the low-fluence limit (1e12) was found to be 100 ns, consistent with a limit from the nuclear spin bath, as established in previous studies¹⁶. As the fluence increases, additional decoherence mechanisms may arise from the increasing $V_{\rm B}^-$ spin concentration and the creation of other spin-active defects. We first consider spectral diffusion experienced by the central spin arising from the spin flips of its neighbors (we neglect any potential contributions that might arise from spin flip-flops due to large inhomogeneous spin linewidth compared to average dipolar coupling strength $\sim 2 \text{ MHz})^{32}$. A quantitative estimate of the spectral diffusion limited T₂ yielded coherence times between 18 µs (for 1e12) to 1.1 µs (for 1e15 sample), based on the measured values of T_1 , so its contribution can be neglected. We next consider so-called 'instantaneous diffusion' which arises from dipolar coupling with *resonant* spins which are also flipped by the Hahn echo π pulse, such that the interactions are not refocused when the echo is formed. The decoherence rate due to instantaneous diffusion can be estimated using the following relation^{32,33}:

$$T_{2,ID}^{-1} = \frac{2\pi^2 \mu_0 h \eta \gamma^2}{9\sqrt{3}} * (\frac{3}{2})$$
 (1)

where η represents the effective concentration of resonant spins contributing (in this case significantly lower than the total defect concentration), μ_0 is the permeability of the free space, h is Planck's constant, and γ is the electron gyromagnetic ratio. As illustrated in Fig. 1(c), the concentration of $V_{\rm R}^$ spins is not a simple linear function of the ion fluence due to varying conversion efficiency, and so we used the PL intensity as a proxy for overall $V_{\rm B}^-$ concentration. Here we assume that for the 1e12 sample, each ion creates \sim 2.5 vacancies on average based on SRIM calculations — see SI). To estimate η , we then scaled this concentration by a factor of 0.18, calculated from the fraction of the total ODMR linewidth addressed by the microwave pulse excitation (see SI). The result is a quantitative estimate of the contribution of instantaneous diffusion to T_2 , which we overlay on the measured values in Fig. 2(c). Based on this model, we expect instantaneous diffusion to begin limiting T_2 for ion fluences above 10^{14} ions/cm², consistent with the measured values. Advanced dynamical decoupling sequences, such as DROID, are required to effectively suppress such dipolar coupling interactions¹⁶.

Having determined key optical and spin properties of the $V_{\rm B}^-$ as a function of ion fluence, we can use these values to understand how $V_{\rm B}^-$ implantation conditions can be optimised for magnetic field sensitivity. Previous studies^{6,28,34–37} have demonstrated DC magnetic sensitivities ranging from $100~\mu T/\sqrt{Hz}$ to $3~\mu T/\sqrt{Hz}$ and predict an estimated sensitivity limit of around $20~n T/\sqrt{Hz}$ under ideal conditions⁶. We calculated the DC sensitivity using the following relation³⁸:

$$\eta_{DC}(T/\sqrt{Hz}) \approx \frac{h}{g\mu_B} \frac{1}{\sqrt{\mathscr{R}} \max \left| \frac{\partial \mathscr{I}}{\partial \nu_0} \right|}$$
(2)

where g denotes the g-factor of the $V_{\rm B}^-$ centers (\sim 2), μ_B is the Bohr magneton, \mathscr{R} is the photon count rate and max $\left|\frac{\partial\mathscr{I}}{\partial v_0}\right|$ represents the slope of the continuous wave ODMR signal (accounting for both contrast and linewidth). The estimated DC magnetic field sensitivity is shown in Fig. 2(d)), indicating an optimal ion fluence between 10^{14} and 10^{15} ions/cm² and a DC sensitivity of around 30 μ T/ $\sqrt{\rm Hz}$. This value reflects a tradeoff between photon count rate, ODMR linewidth broadening, and contrast, all of which contribute to overall magnetic sensitivity performance. We also estimated AC magnetic sensitivity using the following relation^{37,39}:

$$\eta_{\rm AC}({\rm T}/\sqrt{\rm Hz}) \approx \frac{\pi}{2\gamma_e} \frac{1}{C_{\rm max} e^{-(\tau/T_2)} \sqrt{\mathcal{N}}} \frac{\sqrt{t_I + \tau + t_R}}{\tau}, \quad (3)$$

where $C_{\rm max}$ is the maximum measurement contrast, \mathscr{N} is the average photon count collected, γ_e is the electron gyromagnetic ratio, τ is the free evolution time for phase accumulation, optimally set near the coherence time T_2 , and t_I and t_R are, respectively, the initialization and readout times. The optimal ion fluence was identified as 10^{14} ions/cm², leading to AC sensitivity of around $1 \mu T/\sqrt{Hz}$.

Both AC and DC magnetic field sensitivity improve with increasing ion fluence, due to the increased $V_{\rm B}^-$ PL emission. In the case of AC sensing, an optimum is reached around 10¹⁴ ions/cm² which appears to be limited by a drop in coherence time caused by instantaneous diffusion — i.e. by coupling to other, resonant, $V_{\rm B}^-$ spins. In contrast, for DC sensing the limiting factor as ion fluence increases appears to be related to lattice damage and its corresponding effect on the ODMR contrast. This raises the question of whether there is significant migration of $V_{\rm B}^-$ defects at the interface between implanted and unimplanted regions of the hBN flake. In principle, such migration could provide a route to decouple the creation of $V_{\rm B}^-$ spins from the corresponding lattice damage. We next explore such interfaces using PL to monitor $V_{\rm B}^-$ migration and Raman spectroscopy to provide a more general probe of changes in hBN lattice.

We first present Raman spectroscopy obtained well within the ion implanted region, as a function of ion fluence (see Fig. 3). In unimplanted flakes, the characteristic hBN Raman peak (E_{2g} mode) was observed at ~ 1365 cm⁻¹, and we confirmed that any lattice strain induced by transferring the

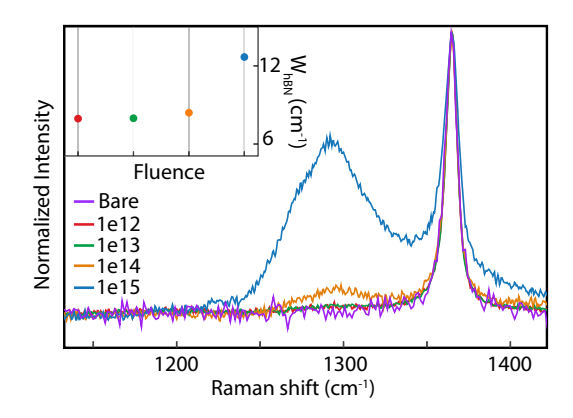


FIG. 3. Raman spectra for different ion-implanted hBN samples and one unimplanted sample. Inset shows the variation in the linewidth of the hBN peak (1365 cm^{-1}) .

flake from a silicon substrate to the gold microstrip was sufficiently negligible that it had no impact on the Raman spectrum (see Fig. SI7). At an ion fluence of 10^{15} ions/cm², broadening of the hBN Raman peak is observed — this can be attributed to increased lattice disorder and the formation of complex defect clusters²¹, and is consistent with the reduction of ODMR contrast and T_1 for V_B^- spins presented above. At fluences of 10^{14} ions/cm² and above, an additional peak near ~ 1295 cm⁻¹ also appears. This peak has been recently attributed to V_B centres^{21,40} (see Fig. SI8).

To investigate migration of defects during FIB ion implantation, we performed PL and Raman spectroscopy measurements along a line cut across the boundary between unimplanted and implanted regions, using a step size of $\sim\!\!1~\mu m.$ In Fig. 4 we show the measurements for samples 1e14 and 1e15, and fit the profiles using a Gaussian error function to obtain the width of the transition region (see SI).

The intensity of the PL signal for both the samples fell across the boundary to the unimplanted region, with a similar width of about $\sim 0.5~\mu m$ (while $\sigma_{laser} \sim 0.3~\mu m$). This rules out significant migration of V_B^- centres toward the unimplanted lattice region under either of the implantation parameters studied. To analyse the spatial variation in the Raman spectra, we focus on two parameters: i) ratio of the intensity of the defect-related peak $I_{\rm V_B}$ and that of the primary hBN peak $I_{\rm hBN}$; and ii) the width of the hBN peak, which increases in the 1e15 sample (see inset of Fig. 3). Each of these Raman features showed a similar step-like function with width $\sigma \sim 0.3~\mu m$ consistent with the beam width used, suggesting that the lattice damage from implantation is limited to the irradiated region for the range of fluences studied here (Fig. 4(c)).

IV. CONCLUSION

FIB implantation of He⁺ ions into hBN is an effective way to pattern $V_{\rm B}^-$ centres which could act as quantum sensors embedded within 2D materials. We have explored how varying the ion fluence influences the properties of $V_{\rm B}^-$ centres relevant

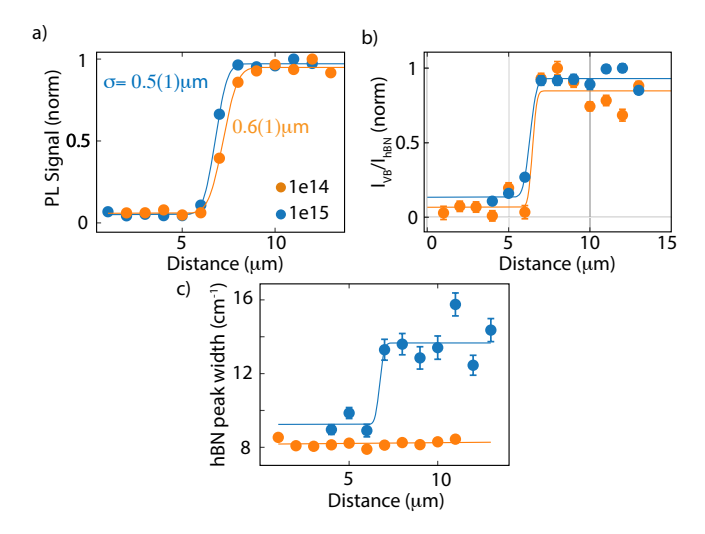


FIG. 4. PL and Raman studies around the boundary between implanted and pristine areas for samples 1e14 and 1e15, respectively. a) Normalized PL signal from V_B^- centres along a line. b) Raman peak intensity ratio I_{V_B}/I_{hBN} (normalized w.r.t. maxima). c) The hBN peak width(FWHM) along the line.

to their application as local magnetic sensors. We identify that with increasing concentration of $V_{\rm B}^-$ centres (through higher ion fluence), the residual defects begin to influence different parameters, ultimately reducing the measurement sensitivity. While higher ion fluence enhances the $V_{\rm B}^-$ centre-related brightness, it also leads to degradation of the spin parameters. The optimal ion implantation condition was determined to be 10¹⁴ ions/cm². Under these conditions, a DC field sensitivity of 30 μ T/ $\sqrt{\text{Hz}}$ was inferred, becoming limited by a reduction in ODMR spin contrast which we attributed to lattice damage induced by the ion implantation. In principle, this DC sensitivity could be improved by decoupling the creation of $V_{\rm R}^$ centres from the formation of lattice defects, however, achieving this through the natural migration of $V_{\rm B}^-$ centres proved unsuccessful. A maximum AC sensitivity of $\sim 1 \ \mu T / \sqrt{Hz}$ was inferred using an ion fluence of 10¹⁴ ions/cm². Here the sensitivity is again limited by a reduction in spin contrast, but now also by dipolar interactions between resonant $V_{\rm B}^-$ spins, posing a more fundamental barrier to further increases. Overall, the insights into these limiting factors in the sensitivity of ion-implanted $V_{\rm R}^-$ sensors will aid in the engineering of 2D magnetic sensor arrays with optimised magnetic sensing properties.

ACKNOWLEDGMENTS

The authors would like to thank Patrick Hogan for helpful discussions and the cleanroom support staff at the London Centre for Nanotechnology for their technical assistance. This work was supported by the Engineering and Physical Sciences Research Council (EPSRC) through the Hub in Quantum Computing and Simulation (Grant No. EP/T001062/1) and through EP/T517793/1. S.D. thanks the Indian Institute of

Technology, Madras, India, and the Science and Engineering Research Board (SERB Grant No. SRG/2023/000322), India, for start-up funding. S.D. and B.M. acknowledge the use of facilities supported by a grant from the Mphasis F1 Foundation given to the Center for Quantum Information, Communication, and Computing (CQuICC). K.W. and T.T. acknowledge support from the JSPS KAKENHI (Grant Numbers 21H05233 and 23H02052), the CREST (JPMJCR24A5), JST and World Premier International Research Center Initiative (WPI), MEXT, Japan.

REFERENCES

- ¹Z. Xu, Z.-q. Yin, Q. Han, and T. Li, "Quantum information processing with closely-spaced diamond color centers in strain and magnetic fields," Optical Materials Express **9**, 4654 (2019).
- ²C. L. Degen, F. Reinhard, and P. Cappellaro, "Quantum sensing," Rev. Mod. Phys. 89, 035002 (2017).
- ³J. M. Taylor, P. Cappellaro, L. Childress, L. Jiang, D. Budker, P. R. Hemmer, A. Yacoby, R. Walsworth, and M. D. Lukin, "High-sensitivity diamond magnetometer with nanoscale resolution," Nature Physics 4, 810 (2008).
- ⁴A. Morello, J. J. Pla, F. A. Zwanenburg, K. W. Chan, K. Y. Tan, H. Huebl, M. Möttönen, C. D. Nugroho, C. Yang, J. A. Van Donkelaar, *et al.*, "Single-shot readout of an electron spin in silicon," Nature **467**, 687 (2010).
- ⁵N. De Zanche, C. Barmet, J. A. Nordmeyer-Massner, and K. P. Pruessmann, "Nmr probes for measuring magnetic fields and field dynamics in mr systems," Magnetic Resonance in Medicine: An Official Journal of the International Society for Magnetic Resonance in Medicine 60, 176 (2008).
 ⁶A. Gottscholl, M. Diez, V. Soltamov, C. Kasper, D. Krauße, A. Sperlich, M. Kianinia, C. Bradac, I. Aharonovich, and V. Dyakonov, "Spin defects in hbn as promising temperature, pressure and magnetic field quantum sen-
- sors," Nature communications **12**, 4480 (2021).

 ⁷N. Aslam, H. Zhou, E. K. Urbach, M. J. Turner, R. L. Walsworth, M. D. Lukin, and H. Park, "Quantum sensors for biomedical applications," Nature Reviews Physics **5**, 157 (2023).
- ⁸M. W. Doherty, N. B. Manson, P. Delaney, F. Jelezko, J. Wrachtrup, and L. C. Hollenberg, "The nitrogen-vacancy colour centre in diamond," Physics Reports **528**, 1 (2013).
- ⁹J.-P. Tetienne, N. Dontschuk, D. A. Broadway, A. Stacey, D. A. Simpson, and L. C. Hollenberg, "Quantum imaging of current flow in graphene," Science advances 3, e1602429 (2017).
- ¹⁰I. Lovchinsky, A. Sushkov, E. Urbach, N. P. de Leon, S. Choi, K. De Greve, R. Evans, R. Gertner, E. Bersin, C. Muller, *et al.*, "Nuclear magnetic resonance detection and spectroscopy of single proteins using quantum logic," Science 351, 836 (2016).
- ¹¹L. P. McGuinness, Y. Yan, A. Stacey, D. A. Simpson, L. T. Hall, D. Maclaurin, S. Prawer, P. Mulvaney, J. Wrachtrup, F. Caruso, *et al.*, "Quantum measurement and orientation tracking of fluorescent nanodiamonds inside living cells," Nature nanotechnology 6, 358 (2011).
- ¹²J. Kitching, "Chip-scale atomic devices," Applied Physics Reviews 5 (2018).
- ¹³A. Gottscholl, M. Kianinia, V. Soltamov, S. Orlinskii, G. Mamin, C. Bradac, C. Kasper, K. Krambrock, A. Sperlich, M. Toth, I. Aharonovich, and V. Dyakonov, "Initialization and read-out of intrinsic spin defects in a van der waals crystal at room temperature," Nature Materials 19, 540 (2020).
- ¹⁴A. Gottscholl, M. Diez, V. Soltamov, C. Kasper, D. Krauße, A. Sperlich, M. Kianinia, C. Bradac, I. Aharonovich, and V. Dyakonov, "Spin defects in hBN as promising temperature, pressure and magnetic field quantum sensors," Nature communications 12, 4480 (2021).
- $^{15}\mathrm{A}.$ Haykal, R. Tanos, N. Minotto, A. Durand, F. Fabre, J. Li, J. H. Edgar, V. Ivády, A. Gali, T. Michel, A. Dréau, B. Gil, G. Cassabois, and V. Jacques, "Decoherence of $\mathrm{V_B^-}$ spin defects in monoisotopic hexagonal boron nitride," Nature Communications 13, 4347 (2022).

- ¹⁶R. Gong, G. He, X. Gao, P. Ju, Z. Liu, B. Ye, E. A. Henriksen, T. Li, and C. Zu, "Coherent dynamics of strongly interacting electronic spin defects in hexagonal boron nitride," Nature Communications 14, 3299 (2023).
- ¹⁷H.-H. Fang, X.-J. Wang, X. Marie, and H.-B. Sun, "Quantum sensing with optically accessible spin defects in van der waals layered materials," Light: Science & Applications 13, 303 (2024).
- ¹⁸N.-J. Guo, W. Liu, Z.-P. Li, Y.-Z. Yang, S. Yu, Y. Meng, Z.-A. Wang, X.-D. Zeng, F.-F. Yan, Q. Li, J.-F. Wang, J.-S. Xu, Y.-T. Wang, J.-S. Tang, C.-F. Li, and G.-C. Guo, "Generation of spin defects by ion implantation in hexagonal boron nitride," ACS Omega 7, 1733 (2022), publisher: American Chemical Society.
- ¹⁹T. Zabelotsky, S. Singh, G. Haim, R. Malkinson, S. Kadkhodazadeh, I. P. Radko, I. Aharonovich, H. Steinberg, K. Berg-Sørensen, A. Huck, *et al.*, "Creation of boron vacancies in hexagonal boron nitride exfoliated from bulk crystals for quantum sensing," ACS Applied Nano Materials 6, 21671 (2023)
- ²⁰M. Kianinia, S. White, J. E. Fröch, C. Bradac, and I. Aharonovich, "Generation of spin defects in hexagonal boron nitride," ACS Photonics 7, 2147 (2020).
- ²¹S. Sarkar, Y. Xu, S. Mathew, M. Lal, J.-Y. Chung, H. Y. Lee, K. Watanabe, T. Taniguchi, T. Venkatesan, and S. Gradečak, "Identifying luminescent boron vacancies in hbn generated using controlled He⁺ ion irradiation," Nano Letters 24, 43 (2023).
- ²²S. Ghaderzadeh, S. Kretschmer, M. Ghorbani-Asl, G. Hlawacek, and A. V. Krasheninnikov, "Atomistic simulations of defect production in monolayer and bulk hexagonal boron nitride under low-and high-fluence ion irradiation," Nanomaterials 11, 1214 (2021).
- ²³T. Taniguchi and K. Watanabe, "Synthesis of high-purity boron nitride single crystals under high pressure by using Ba–BN solvent," Journal of crystal growth 303, 525–529 (2007).
- ²⁴X. Gao, B. Jiang, A. E. Llacsahuanga Allcca, K. Shen, M. A. Sadi, A. B. Solanki, P. Ju, Z. Xu, P. Upadhyaya, Y. P. Chen, *et al.*, "High-contrast plasmonic-enhanced shallow spin defects in hexagonal boron nitride for quantum sensing," Nano Letters 21, 7708 (2021).
- ²⁵ X. Gao, S. Vaidya, K. Li, P. Ju, B. Jiang, Z. Xu, A. E. L. Allcca, K. Shen, T. Taniguchi, K. Watanabe, *et al.*, "Nuclear spin polarization and control in hexagonal boron nitride," Nature Materials 21, 1024 (2022).
- ²⁶I. N. Gracheva, F. F. Murzakhanov, G. V. Mamin, M. A. Sadovnikova, B. F. Gabbasov, E. N. Mokhov, and M. R. Gafurov, "Symmetry of the hyperfine and quadrupole interactions of boron vacancies in a hexagonal boron nitride," The Journal of Physical Chemistry C 127, 3634 (2023).
- ²⁷P. W. Percival and J. S. Hyde, "Phase cycling in pulsed electron paramagnetic resonance," Review of Scientific Instruments 46, 1552 (1975).

- ²⁸ A. J. Healey, P. Singh, I. O. Robertson, C. Gavin, S. C. Scholten, D. A. Broadway, P. Reineck, H. Abe, T. Ohshima, M. Kianinia, I. Aharonovich, and J.-P. Tetienne, "Optimisation of electron irradiation for creating spin ensembles in hexagonal boron nitride," Materials for Quantum Technology 4, 035701 (2024).
- ²⁹H. Liang, Y. Chen, C. Yang, K. Watanabe, T. Taniguchi, G. Eda, and A. A. Bettiol, "High sensitivity spin defects in hbn created by high-energy He beam irradiation," Advanced Optical Materials 11, 2201941 (2023).
- ³⁰K. Li, V. D. Dergachev, I. D. Dergachev, S. Zhang, S. A. Varganov, and Y. Ping, "Excited-state dynamics and optically detected magnetic resonance of solid-state spin defects from first principles," Phys. Rev. B 110, 184302 (2024).
- ³¹N. J. Guo, W. Liu, Z. P. Li, Y. Z. Yang, S. Yu, Y. Meng, Z. A. Wang, X. D. Zeng, F. F. Yan, Q. Li, J. F. Wang, J. S. Xu, Y. T. Wang, J. S. Tang, C. F. Li, and G. C. Guo, "Generation of spin defects by ion implantation in hexagonal boron nitride," ACS Omega 7, 1733 (2022).
- ³²H.-J. Lim, S. Welinski, A. Ferrier, P. Goldner, and J. J. L. Morton, "Coherent spin dynamics of ytterbium ions in yttrium orthosilicate," Phys. Rev. B 97, 064409 (2018).
- ³³A. Schweiger and G. Jeschke, *Principles of pulse electron paramagnetic resonance* (Oxford university press, 2001).
- ³⁴F. Ren, Y. Wu, and Z. Xu, "Creation and repair of luminescence defects in hexagonal boron nitride by irradiation and annealing for optical neutron detection," Journal of Luminescence 261, 119911 (2023).
- ³⁵M. Huang, J. Zhou, D. Chen, H. Lu, N. J. McLaughlin, S. Li, M. Alghamdi, D. Djugba, J. Shi, H. Wang, *et al.*, "Wide field imaging of van der waals ferromagnet Fe₃GeTe₂ by spin defects in hexagonal boron nitride," Nature communications 13, 5369 (2022).
- ³⁶F. Zhou, Z. Jiang, H. Liang, S. Ru, A. A. Bettiol, and W. Gao, "Dc magnetic field sensitivity optimization of spin defects in hexagonal boron nitride," Nano Letters 23, 6209 (2023).
- ³⁷R. Gong, X. Du, E. Janzen, V. Liu, Z. Liu, G. He, B. Ye, T. Li, N. Y. Yao, J. H. Edgar, *et al.*, "Isotope engineering for spin defects in van der waals materials," Nature Communications 15, 104 (2024).
- ³⁸A. Dréau, M. Lesik, L. Rondin, P. Spinicelli, O. Arcizet, J.-F. Roch, and V. Jacques, "Avoiding power broadening in optically detected magnetic resonance of single nv defects for enhanced dc magnetic field sensitivity," Physical Review B—Condensed Matter and Materials Physics 84, 195204 (2011).
- ³⁹J. F. Barry, J. M. Schloss, E. Bauch, M. J. Turner, C. A. Hart, L. M. Pham, and R. L. Walsworth, "Sensitivity optimization for NV-diamond magnetometry," Reviews of Modern Physics 92, 015004 (2020).
- ⁴⁰G. Venturi, S. Chiodini, N. Melchioni, E. Janzen, J. H. Edgar, C. Ronning, and A. Ambrosio, "Selective generation of luminescent defects in hexagonal boron nitride," Laser & Photonics Reviews 18, 2300973 (2024).

Supplementary Information

1 Sample Fabrication

Gold strip-lines were fabricated on bare SiO_2/Si substrates using direct-write photolithography. 5nm of chrome was evaporated as an adhesion layer, followed by 210nm of gold by electron beam evaporation. Lift-off was performed in DMSO at 65°C for 10 minutes. hBN flakes used in this study were grown under high pressure and high temperature [8]. The flakes were first exfoliated on a bare SiO_2/Si substrate and picked up by a PC stamp, aligned with an optical microscope and deposited on the gold strip-line [4]. The PC stamp was melted onto the gold strip-line at 180°C and residual PC was dissolved in chloroform. The hBN-gold strip-line structures were cleaned by acetone and IPA.

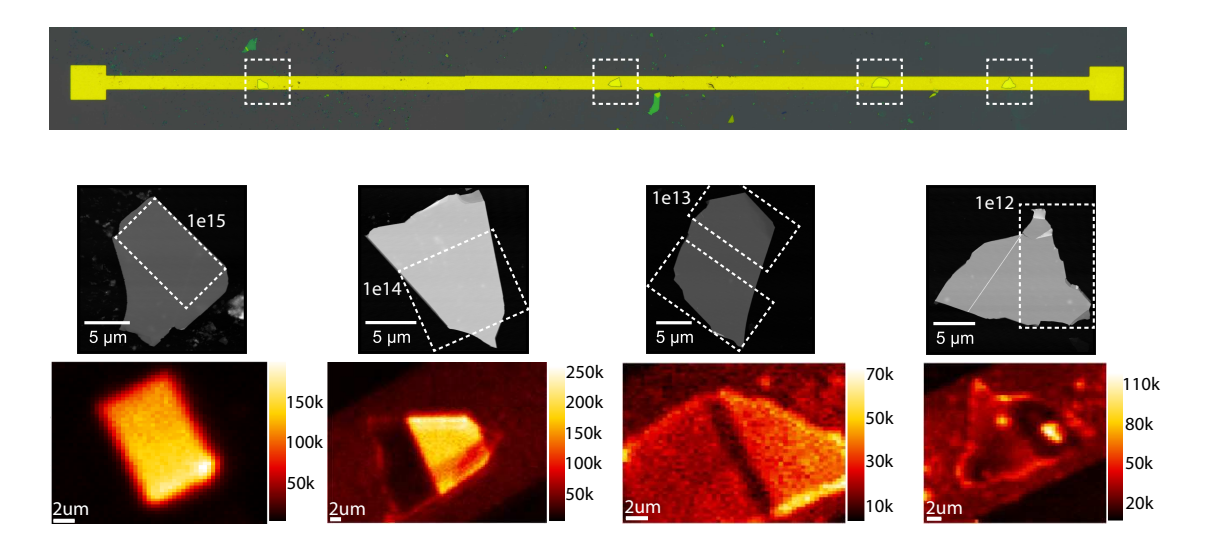


Figure 1: Optical Image of the gold microstrip (not to scale), displaying all flakes implanted with varying ion fluence. Below this, Atomic Force Microscopy (AFM) images and the corresponding confocal microscope images of the same flakes are shown. The dotted regions in the AFM images indicate the implanted area, which is also distinguishable in the confocal images through the change in photon counts.

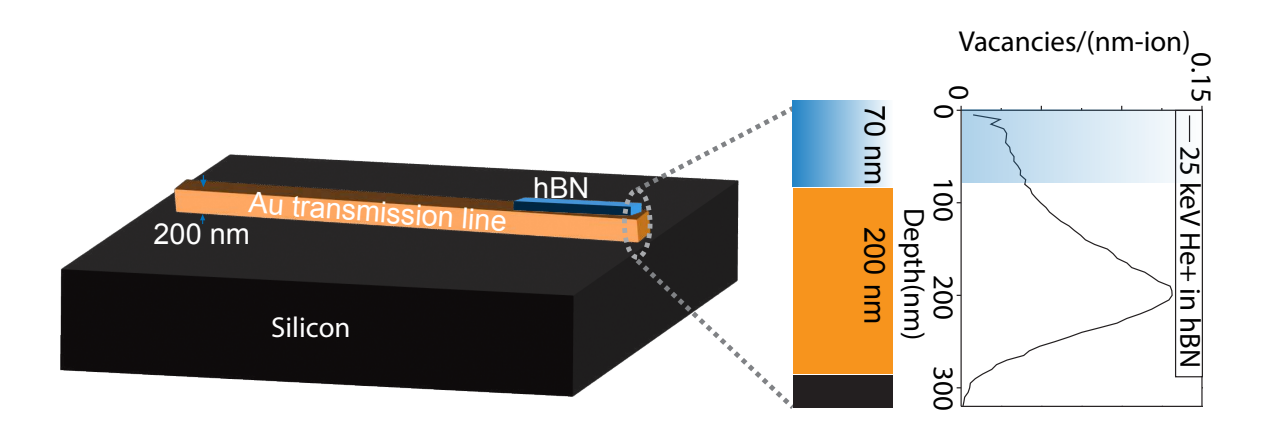


Figure 2: Cartoon representation of sample configuration. The hBN nanoflakes are placed on a ~ 200 nm thick gold transmission line fabricated on the top of a silicon substrate. The vacancy profile, estimated using SRIM simulations, has also been shown.

The concentration of boron vacancies was estimated using SRIM simulations, which revealed that each incident He⁺ ion generates approximately 22 vacancies along its full penetration depth (maximum range \sim 270 nm) in the hBN lattice. From the calculated vacancy

profile (Fig. 2), we estimate that about 12% of these vacancies are produced within the top 70 nm—the typical thickness of the hBN nanoflakes studied here—corresponding to ~ 2.5 boron vacancies per implanted He⁺ ion.

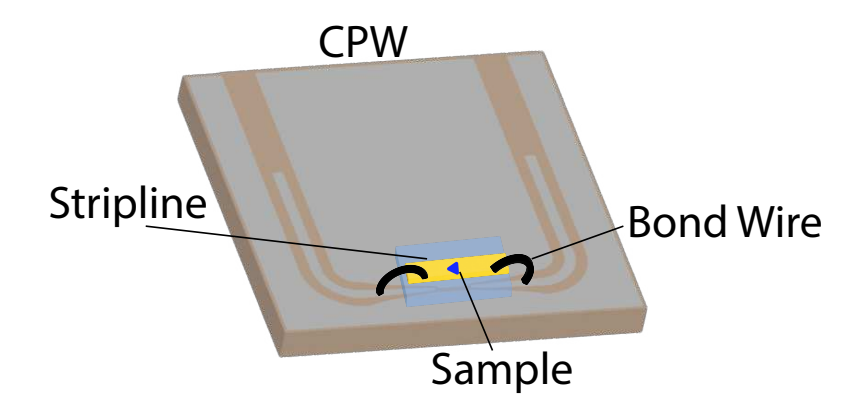


Figure 3: The combined coplanar waveguide (CPW) microstrip design is used to apply microwaves for the manipulation of V_B^- defects in these flakes. The CPW features a central constriction, and the gap between the conductor arms and is based on a previously developed design within the group.[1]

2 Model System Hamiltonian

We consider a model Hamiltonian describing a single V_B^- defect (S = 1) interacting with the three first-shell nitrogen spin bath(¹⁴N) via hyperfine interactions. The Hamiltonian of the composite system can be written as:

$$H = D\left(S_z^2 - \frac{2}{3}\right) + E\left(S_y^2 - S_x^2\right) + \gamma_e \mathbf{B} \cdot \mathbf{S} + \sum_{i=1}^3 \mathbf{S} \cdot \mathbf{A}^i \cdot \mathbf{I}^i + \sum_{i=1}^3 \gamma_n^i \mathbf{B} \cdot \mathbf{I}^i + \sum_{i=1}^3 \mathbf{I}^i \cdot \mathbf{Q}^i \cdot \mathbf{I}^i.$$
(1)

Here, S and I are the electron and nuclear spin operators, respectively. D represents the zero-field splitting (ZFS) term, while E accounts for the electric field susceptibility. γ_e and γ_n denote the electron and nuclear gyromagnetic factors, respectively. A is the hyperfine interaction tensor, Q is the quadrupole interaction tensor, and B represents the externally

applied magnetic field (Zeeman interaction). The coupling parameters used in our numerical calculations are listed in Table 1.

	A_{xx}	A_{yy}	A_{zz}	A_{xy}	Q_{xx}	Q_{yy}	Q_{zz}	Q_{xy}
N^1	46.944	90.025	48.158	0	-0.46	0.98	-0.52	0
N^2	79.406	58.170	48.159	-18.391	0.62	-0.1	-0.52	-0.623
N^3	79.406	58.170	48.159	18.391	0.62	-0.1	-0.52	0.623

Table 1: Hyperfine and quadrupolar tensor elements used in the numerical calculations. [2, 3]

3 Optically Detected Magnetic Resonance (ODMR) Simulation

We used QuTiP to compute the transition frequencies and probabilities based on Fermi's Golden Rule. Since the amplitude of transitions is directly proportional to the transition probability, we introduced an additional free parameter alongside D, E, and the linewidth. To simulate the optically detected magnetic resonance (ODMR) spectrum, we assumed all transitions follow a Lorentzian profile given by:

$$L(\omega, A, \omega_0, \Delta\omega) = A \frac{(\Delta\omega/2)}{(\omega - \omega_0)^2 + (\Delta\omega/2)^2}$$
 (2)

where ω is the frequency, A is the amplitude, ω_0 is the central frequency, and $\Delta\omega$ is the full width at half maximum (FWHM). Based on this model, we used SciPy's curve-fitting functionality to fit the theoretical ODMR spectrum to experimental data, allowing us to extract the parameters D, E, and the linewidth.

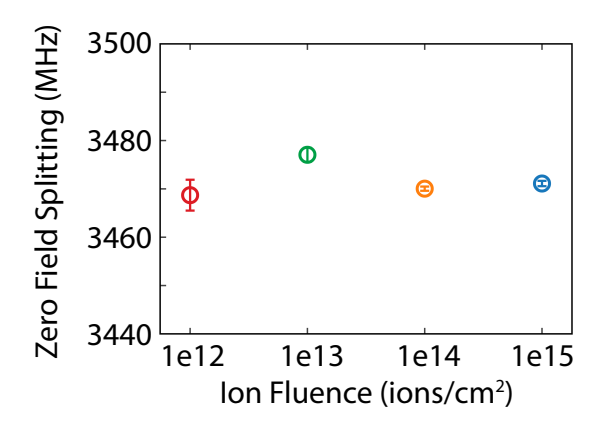


Figure 4: Zero field splitting parameter(D) extracted from PODMR fitting, with varying ion fluence.

4 Coherence time measurements

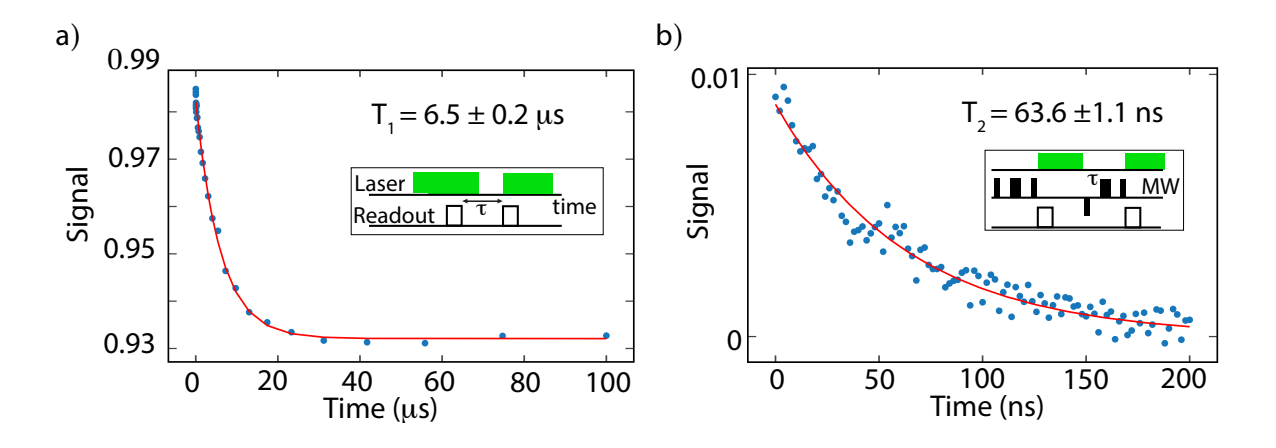


Figure 5: Fitting of coherence time data for flake 1e15 with insets showing the pulse sequences used. a) T_1 data b) Hahn Echo T_2

5 Instantaneous Spin Diffusion

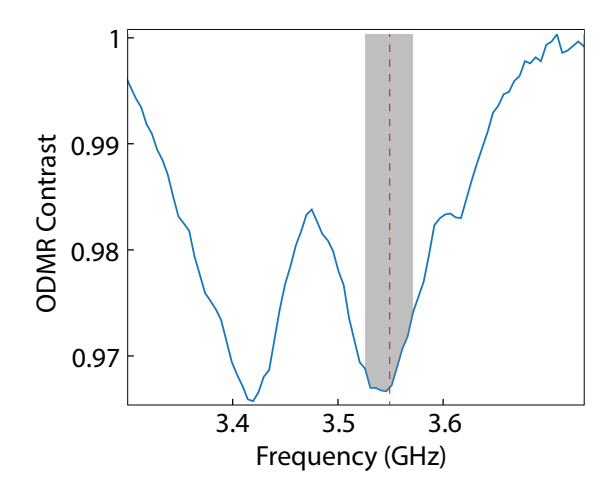


Figure 6: PODMR data for sample 1e15, with the red line indicating the MW frequency used for the Hahn Echo experiment and the shaded grey region representing the calculated bandwidth of the pulse.

Based on area-under-the-curve calculations, we estimate that the Hahn echo π pulse addresses approximately 18% of the total spin ensemble. Interactions among these addressed spins are not refocused by the π pulse and therefore contribute to instantaneous spin diffusion.

6 Material characterization

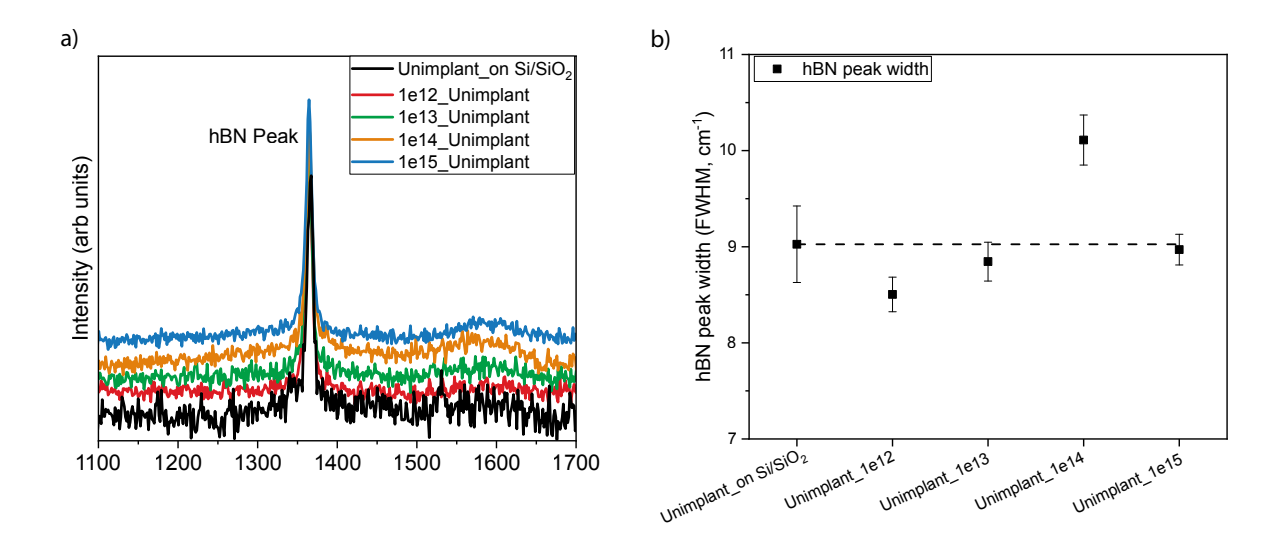


Figure 7: (a) Raman spectra of different hBN nanoflakes (placed on gold transmission line) before FIB implantation. The Raman spectrum of an unimplanted hBN nanoflake, placed on a Silicon substrate (with a native thermal oxide layer), has been shown for comparison.

(b) The hBN peak width for different unimplanted nanoflakes.

To further investigate the origin of the peak $\sim 1295~\rm cm^{-1}$, multiwavelength Raman spectroscopy was performed using laser wavelengths from 457 nm to 785 nm (see Fig.8). The peak intensity increases with excitation wavelength up to $\sim 500~\rm nm$ and decreases thereafter, suggesting a resonance maximum around 500 nm, consistent with previous findings [7]. This trend contrasts with typical hBN or cBN Raman behavior, which peaks in the UV regime due to their wide bandgap ($\sim 200~\rm nm$)[5].

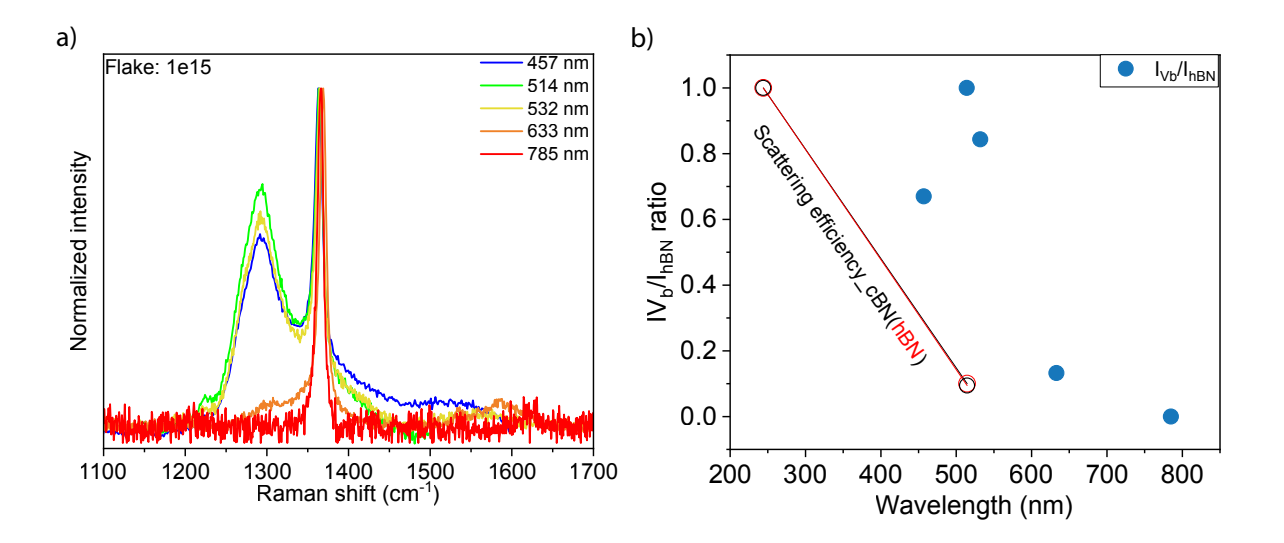


Figure 8: Normalized Raman spectra under different laser excitation wavelengths between 457 - 785 nm. (b) The I_{Vb}/I_{hBN} ratio for different laser excitation wavelengths. The maxima for I_{Vb}/I_{hBN} was found to be at 514 nm. To compare the trend with wavelength dependent Raman signal intensity of cBN and hBN, we have compared the Raman scattering efficiency of both phases (shown as the black and red dotted lines). The scattering efficiency is taken as the proxy of Raman signal intensity for comparison.[6]

7 Migration Analysis

We modeled the expected distribution of defects under Gaussian beam illumination using the following function:

$$f(x) = \frac{1}{2} \left[1 + \operatorname{erf}\left(\frac{x - x_0}{\sqrt{2}\sigma}\right) \right] \cdot h + C_0, \tag{3}$$

where x_0 is the step offset, σ is the standard deviation of the Gaussian profile, h is the step height, and C_0 is the baseline offset.

The width of the underlying defect distribution can then be extracted from the measured profile using

$$\sigma_{\text{distribution}} = \sqrt{\sigma_{\text{measured}}^2 - \sigma_{\text{laser}}^2},$$
 (4)

where σ_{measured} is the standard deviation obtained from fitting the Gaussian error function, and σ_{laser} is the standard deviation of the laser's Gaussian beam profile.

References

- [1] Felix A. B. Donaldson. Nuclear spin ancilla-assisted readout of a single NV centre in an AFM probe. Ph.d. thesis, University College London, 2024.
- [2] Xingyu Gao, Sumukh Vaidya, Kejun Li, Peng Ju, Boyang Jiang, Zhujing Xu, Andres E Llacsahuanga Allcca, Kunhong Shen, Takashi Taniguchi, Kenji Watanabe, et al. Nuclear spin polarization and control in hexagonal boron nitride. *Nature Materials*, 21(9):1024, 2022.
- [3] Irina N Gracheva, Fadis F Murzakhanov, Georgy V Mamin, Margarita A Sadovnikova, Bulat F Gabbasov, Evgeniy N Mokhov, and Marat R Gafurov. Symmetry of the hyperfine and quadrupole interactions of boron vacancies in a hexagonal boron nitride. *The Journal* of Physical Chemistry C, 127(7):3634, 2023.
- [4] D G Purdie, NM Pugno, T Taniguchi, K Watanabe, AC Ferrari, and Antonio Lombardo. Cleaning interfaces in layered materials heterostructures. *Nature communications*, 9(1):5387, 2018.
- [5] S Reich, AC Ferrari, R Arenal, A Loiseau, I Bello, and J Robertson. Resonant raman scattering in cubic and hexagonal boron nitride. *Physical Review B—Condensed Matter and Materials Physics*, 71(20):205201, 2005.
- [6] Stephanie Reich, Andrea C. Ferrari, Raul Arenal, Annick Loiseau, Igor Bello, and John Robertson. Resonant raman scattering in cubic and hexagonal boron nitride. *Physical Review B*, 71(20):205201, 2005.
- [7] Soumya Sarkar, Yue Xu, Sinu Mathew, Manohar Lal, Jing-Yang Chung, Hae Yeon Lee, Kenji Watanabe, Takashi Taniguchi, Thirumalai Venkatesan, and Silvija Gradečak. Identifying luminescent boron vacancies in hBN generated using controlled He⁺ ion irradiation. *Nano Letters*, 24(1):43, 2023.

[8] Takashi Taniguchi and Kenji Watanabe. Synthesis of high-purity boron nitride single crystals under high pressure by using Ba–BN solvent. *Journal of crystal growth*, 303(2):525, 2007.